

# Lawrence Berkeley National Laboratory

## LBL Publications

### Title

Characterizing regional-scale temporal evolution of air dose rates after the Fukushima Daiichi Nuclear Power Plant accident

### Permalink

<https://escholarship.org/uc/item/9v67n1md>

### Authors

Wainwright, Haruko M

Seki, Akiyuki

Mikami, Satoshi

et al.

### Publication Date

2019-12-01

### DOI

10.1016/j.jenvrad.2018.09.006

Peer reviewed

# 1Characterizing Regional-Scale Temporal Evolution of Air Dose Rates 2After the Fukushima Dai-ichi Nuclear Power Plant Accident

3

## 4Abstract

5In this study, we quantify the temporal changes of air dose rates in the  
6regional scale around the Fukushima Dai-ichi Nuclear Power Plant in Japan,  
7and predict the spatial distribution of air dose rates in the future. We first  
8apply the Bayesian geostatistical method developed by Wainwright et al.  
9(2017) to integrate multiscale datasets including ground-based walk and car  
10surveys, and airborne surveys, all of which have different scales, resolutions,  
11spatial coverage, and accuracy. This method is based on geostatistics to  
12represent spatial heterogeneous structures, and also on Bayesian  
13hierarchical models to integrate multiscale, multi-type datasets in a  
14consistent manner. We apply this method to the datasets from three years:  
152014 to 2016. The temporal changes among the three integrated maps  
16enables us to characterize the spatiotemporal dynamics of radiation air dose  
17rates. The data-driven ecological decay model is then coupled with the  
18integrated map to predict future dose rates. Results show that the air dose  
19rates are decreasing consistently across the region. While slower in the  
20forested region, the decrease is particularly significant in the town area. The  
21decontamination has contributed to significant reduction of air dose rates. By  
222026, the air dose rates will continue to decrease, and the area above 3.8  
23 $\mu\text{Sv/h}$  will be almost fully contained within the non-residential forested zone.



## 251. Introduction

26 Six years has passed since the radionuclide release occurred at the  
27 Fukushima Dai-ichi Nuclear Power Plant (FDNPP). During the accident,  
28 radionuclides were deposited on soil and plants through wet and dry  
29 deposition (Tanaka, 2012). Radiocesium ( $^{134}\text{Cs}$  and  $^{137}\text{Cs}$ ) is currently the  
30 main contaminant in the environment (Saito, 2016). Over the past six years,  
31 the region around FDNPP has experienced remarkable recovery. The current  
32 evacuation designated area has shrunk to 370 km<sup>2</sup> in April 2017, which is  
33 2.7% of the Fukushima Prefecture (Fukushima Prefectural Government,  
34 2017). The extensive decontamination effort has played a critical role in this  
35 recovery process (Yasutaka et al., 2013). In addition, many studies have  
36 reported that the decrease in the air dose rates - including the reduction  
37 associated with radiocesium transport in the environment - has been  
38 accelerated compared to the physical decay (Kinase et al., 2014; Kinase et  
39 al., 2017). It has been found that the air dose rates have reduced to around  
40 one fourth in the undisturbed flat land and one fifth on the urban roads in the  
41 first four years (Saito, 2016).

42

43 An extensive monitoring program has been established after the accident  
44 and still continues to this day (Mikami et al., 2015a; Saito and Onda, 2015).  
45 One of the main goals in the monitoring program has been to map radiation  
46 dose rates, i.e., the ambient dose equivalent rates, in a regional scale based  
47 on the datasets collected by different agencies (Saito, 2016). The datasets

48have been carefully archived and made accessible to the public (Seki et al.,  
492014). The monitoring program has been playing a central role towards  
50ensuring the public safety and preparing for decontamination efforts and  
51residents' return. In addition, monitoring has provided information critical to  
52understand the transport behavior of radiocesium in the environment (Saito,  
532016).

54

55There are a variety of monitoring platforms and data available in the regions.  
56In addition to continuous-time monitoring posts, spatially extensive datasets  
57include airborne, car and walk surveys once or twice a year. Car surveys are  
58based on a GPS-aided mobile radiation monitoring system, the Kyoto  
59University Radiation Mapping system (KURAMA), which has been used  
60extensively to characterize the distribution of air dose rates along the roads  
61in real time (Andoh et al., 2015; Tanigaki et al., 2015). In walk surveys,  
62people carry around the same KURAMA-II systems in small streets and  
63various places outside where people walk around, so that the potential  
64external dose outside can be mapped in detail. Airborne surveys have  
65provided vital information to map the air dose rates across the region (Torii  
66et al., 2012). These measurements of air dose rates have been also  
67considered an excellent proxy for radiocesium contamination in soil at flat  
68fields (Mikami et al., 2015b; Saito et al., 2015).

69

70Changes in air dose rates have been characterized extensively based on  
71these monitoring datasets, aiming to describe and predict the reduction of  
72radiation air dose rates in the environment (Kinase et al., 2014; Kinase et al.,  
732015). Although there have been efforts to model radionuclide transport  
74mechanistically in the near surface environment (e.g., Kitamura et al., 2014;  
75Wei et al., 2017), the exact prediction has been challenging, since the  
76transport involves numerous spatially and temporally heterogeneous factors  
77difficult to measure over time and space. In particular, the radiocesium  
78transport in urban areas is known to be dictated by anthropologic impacts  
79such as traffic and human movements (Andoh et al., 2015). Such enhanced  
80reduction in air dose rates can be defined as environmental or ecological  
81decay, and described by data-driven models with the environmental or  
82ecological half-life (Peles et al., 2002). In the Fukushima region, a significant  
83effort was made to develop data-driven models and to compute the rate of  
84ecological decay (e.g., Kinase et al., 2014; 2017).

85

86However, it has been difficult to quantify the heterogeneity of environmental  
87decay in the regional scale, since spatially extensive airborne survey  
88datasets often have discrepancy with the ground-based measurements and  
89have a larger uncertainty due to the large measurement footprints, and  
90atmospheric effects. In addition, the complex terrain in the forested  
91mountainous region is considered to increase uncertainty (Torii et al., 2012).  
92Recently, Wainwright et al. (2017) developed a Bayesian hierarchical

93 modeling approach to integrate multiscale datasets (i.e., car, walk and  
94 airborne surveys), and also to estimate the spatial distribution of air dose  
95 rates in high resolution over space. They estimated the air dose rates  
96 equivalent to walk surveys, since walk surveys represent the exposure of an  
97 average person walking outside. The integrated air dose-rate maps are more  
98 accurate than the airborne data alone, having less bias and uncertainty.

99

100 In this study, our goals are (1) to quantify the temporal changes of air dose  
101 rates in the regional scale, (2) to identify the characteristics of environmental  
102 decay rates depending on land-use, and (3) to predict air dose rates in the  
103 future. We focus on the evacuation designated area and the region where  
104 the restriction order was recently lifted in March 2017. We first extend the  
105 approach by Wainwright et al. (2017) to a larger area covering this region,  
106 and create multiple integrated maps every year at the time when the  
107 airborne datasets were collected. Then we characterize the changes in air  
108 dose rates, including the effect of decontamination in villages and urban  
109 areas. Our results are expected to help inform efforts to plan for the  
110 residents' return and decontamination efforts in the area currently  
111 designated for evacuation.

112

## 113 **2. Materials and methods**

### 114 **2.1. Site and data**

115The area of interest in this study includes the current evacuation designated  
116area, and the area where the restriction order was recently lifted in March  
1172017 (Fig. 1a). It extends from the FDNPP location to the northwest, following  
118the radioactive plume during the accident. This area –approximately 730 km<sup>2</sup>  
119– is mostly forested with 16 % of the land used for agriculture, 83 % forested,  
120and just 1 % representing urban use, according to the high-resolution land-  
121use and land-cover map of Japan (version 14.02) created by Japan Aerospace  
122Exploration Agency (Takahashi et al., 2013). This area extends from the  
123coast towards the mountains, with the altitude ranging from 0 m to about  
1241000 m above the sea level.

125

126In the same manner as Wainwright et al. (2017), we used the three types of  
127air dose rate datasets compiled by Japan Atomic Energy Agency (JAEA). The  
128car survey datasets used in our study were acquired through the publically  
129available database (<http://emdb.jaea.go.jp/emdb/en/>) and collected using the  
130KURAMA-II systems along the major roads. The KURAMA-II system included a  
131CsI(Tl) scintillation detector, GPS and a software-designed control device  
132(Tsuda et al., 2015). The calibration was done using gamma rays from  
133radioisotope sources at the Facility of Radiation Standard and the Instrument  
134Calibration Facility in JAEA. The dose rate was measured automatically along  
135with the GPS location every three seconds, while the car was moving in the  
136legal speed or along with the traffic. The datasets were averaged within the  
137100 m-by-100 m mesh. The walk survey datasets were provided by JAEA



138after averaging the data values within the 20 m-by-20 m mesh. The walk  
139survey used the KURAMA-II system as well. In addition, we used the  
140publically available air survey datasets that were calibrated to the equivalent  
141dose rates to the one 1m-above ground (Torii et al., 2012). The datasets  
142were given within the 250 m-by-250 m mesh after interpolation using the  
143IDW (inverse distance weighted) method.

144

145Although the types of datasets are the same as those used in Wainwright et  
146al. (2017), there are some differences. The dose rate is generally higher in  
147the evacuation designated area than Fukushima City used for the estimation  
148in the previous study. It is known that the air dose rate reduction tendencies  
149are different in the evacuation zone due to the lack of human activity (Saito,  
1502016). In addition, the evacuation designated area has a larger spatial  
151coverage of forested areas with less human activity. The spatial coverage of  
152car and walk surveys is therefore limited compared to the spatial data  
153coverage in Fukushima City.

154

## 1552.2. Methodology

156We use the data integration methodology developed by Wainwright et al.  
157(2017). Although the detailed description is available in Wainwright et al.  
158(2017), we briefly summarize the methodology here for completeness. Our  
159data integration is based on a Bayesian hierarchical model, which consists of  
160statistical sub-models: data models and process models (Wikle et al., 2001).  
161The process models—in this context—describe the spatial pattern (or map) of  
162air dose rates within the domain, representing the spatial trend and  
163heterogeneity of contamination. We use a geostatistical model to describe  
164this spatial pattern (Deutsch and Journel, 1998; Diggle and Ribeiro, 2007).  
165The goal is to estimate the air dose rates equivalent to walk surveys, since  
166walk surveys represent the exposure of an average person walking outside.  
167

168To develop an integrated map, we denote the radiation dose rate at  $i$ -th pixel  
169by  $y_i$ , where  $i = 1, \dots, n$ . We also denote three datasets by three vectors,  
170representing the airborne survey data  $\mathbf{z}_A$  (each data point is represented by  
171 $\mathbf{z}_{A,j}$ , where  $j = 1, \dots, m_A$ ), car survey data  $\mathbf{z}_C$  (each data point is represented by  
172 $\mathbf{z}_{C,j}$ , where  $j = 1, \dots, m_C$ ), and walk survey data (each data point is represented  
173by  $\mathbf{z}_{W,j}$ , where  $j = 1, \dots, m_W$ ). The goal is to estimate the posterior distribution  
174of the radiation dose-rate map  $\mathbf{y}$  (i.e., the vector representing the radiation  
175dose rates at all the pixels) conditioned on these three datasets ( $\mathbf{z}_A$ ,  $\mathbf{z}_C$  and  
176 $\mathbf{z}_W$ ), written as  $p(\mathbf{y} | \mathbf{z}_A, \mathbf{z}_C, \mathbf{z}_W)$ . By applying Bayes' rule, we can re-write this  
177posterior distribution as:

178  $p(\mathbf{y} | \mathbf{z}_A, \mathbf{z}_C, \mathbf{z}_W) \propto p(\mathbf{z}_A | \mathbf{y}) p(\mathbf{z}_C | \mathbf{y}) p(\mathbf{y} | \mathbf{z}_W)$

179 (1)

180 We assume that the datasets are conditionally independent of each other,  
181 given the air dose rate distribution  $\mathbf{y}$ .

182

183 Detailed descriptions of mathematical formulation are available in  
184 Wainwright et al. (2017). The first distributions  $p(\mathbf{z}_A | \mathbf{y})$  and  $p(\mathbf{z}_C | \mathbf{y})$   
185 represent the data models to describe the low-resolution data (i.e., airborne  
186 and car survey data) as a function of the air dose rate map  $\mathbf{y}$ . The spatial  
187 average functions are included in these conditional distributions. For spatial  
188 averaging, Wainwright et al. (2017) have compared different averaging  
189 schemes based on the observation in the datasets. Based on their results,  
190 we use simple averaging for car survey data within the 100-meter radius. We  
191 use weighted averaging to represent the large footprint of airborne survey,  
192 the weight of which is computed by the radiation transport simulations  
193 (Malins et al., 2016). The third distribution  $p(\mathbf{y} | \mathbf{z}_W)$  represents the process  
194 model (i.e., geostatistical model) to describe the spatial pattern given the  
195 measured dose rates in the walk surveys. We also assume that the  
196 parameters in the data and process models are estimated and well-  
197 constrained through the exploratory data analysis and hence they are fixed  
198 during this Bayesian estimation. The correlation parameters are determined  
199 for each land-use class. After all the sub-models are defined and  
200 parameterized, the air dose rate map can be computed according to Eq. (1).

201 We have defined different parameters in the data and process models for  
202 different land-cover types (Table S1 and S2).

203

204 To characterize the temporal changes and their spatial variability, we define  
205 the dose rate reduction by the log-difference of the air dose rates in each  
206 year in a similar manner as Kinase et al. (2015). In this study, we first apply  
207 this integration method separately to the datasets in each year from 2014 to  
208 2016 for creating three integrated maps at the 50-meter resolution. The  
209 geostatistical and correlation parameters are determined separately for each  
210 year based on available datasets. This process provides snapshots of  
211 spatiotemporal dynamics of air dose rates in the region. We then analyze the  
212 spatial heterogeneity of the dose rate reduction to see whether it has been  
213 affected by decontamination or whether it is dependent on land-use type.

214

215 We then temporally extrapolate the air dose rates by coupling this integrated  
216 map in 2016 with the data-driven ecological decay model developed by  
217 Kinase et al. (2014; 2017). Since we assume the 2016 map as the initial  
218 condition, we can predict the air dose rate at time  $t_2$  based on the known  
219 dose rate map at time  $t_1$  ( $t_1 = 2016$ ). We modify the equation in Kinase et al.  
220 (2014) as:

221

$$\frac{D(t_2) - D_{BG}}{D(t_1) - D_{BG}} = \frac{\left\{ f_{fast} 0.5^{t_2/T_{fast}} + (1 - f_{fast}) 0.5^{t_2/T_{slow}} \right\} k e^{-\lambda_{134} t_2} + e^{-\lambda_{137} t_2}}{\left\{ f_{fast} 0.5^{t_1/T_{fast}} + (1 - f_{fast}) 0.5^{t_1/T_{slow}} \right\} k e^{-\lambda_{134} t_1} + e^{-\lambda_{137} t_1}} \quad (2)$$

222where  $\dot{D}(t)$  is the air dose rate at time  $t$ ,  $\dot{D}_{BG}$  is the background dose rate  
223[ $\mu\text{Sv/h}$ ],  $f_{fast}$  is the fractional distribution of fast elimination component,  $\lambda_{fast}$  is  
224the ecological half-life for the fast elimination component,  $\lambda_{slow}$  is the  
225ecological half-life for the slow elimination component,  $\dot{D}_0$  is the ambient dose  
226equivalent rate ratio of  $^{134}\text{Cs}$  and  $^{137}\text{Cs}$  at time zero,  $\lambda_{134}$  is the physical decay  
227constant of  $^{134}\text{Cs}$ , and  $\lambda_{137}$  is the physical decay constant of  $^{137}\text{Cs}$ . In addition  
228to the mean integrated map of radiation dose rates in 2016, we use the  
229decay parameters determined through fitting in Kinase et al. (2017) or the  
230same assumed parameters (Table S3) to create a predicted air dose rate  
231map in 2026.

232

### 2333. Results and discussions

234The 2016 data on air dose rates are shown as an example in Fig. 2, which  
235are the latest datasets currently available. Although the airborne survey (Fig.  
2362a) has the complete coverage of this region, the discrepancies are apparent  
237between the airborne data and other ground-based measurements. In  
238particular, the airborne data show higher air dose rates compared to the car  
239and walk survey data in the same regions. On the other hand, the car survey  
240data are limited along the major roads (Fig. 2b), while the walk survey data  
241are clustered in multiple small areas (Fig. 2c). The ground-based surveys  
242alone cannot capture the spatial heterogeneity of the air dose rate  
243distribution in the regional scale.

244

245The comparison among different types of datasets (Fig. 3 and 4) shows the  
246discrepancy of air dose rates among them. Figure 3 shows that the car and  
247walk survey datasets are along the one-to-one lines, and highly correlated  
248(the correlation coefficients of 0.96 to 0.97), when co-located data points are  
249selected. Simple spatial averaging of walk survey data around each car data  
250point improves the correlation coefficients to 0.99. The comparison between  
251the airborne and walk survey datasets (Fig. 4) shows that the airborne  
252survey data values are higher than the walk survey data even at the same  
253locations, although the two types of data are significantly correlated (the  
254correlation coefficients of 0.93 to 0.96). Weighted spatial averaging of the  
255walk survey data around each airborne data point improves the correlation  
256significantly to the correlation coefficients of 0.96 - 0.99. Several studies  
257have found that the airborne survey data are consistently higher than co-  
258located ground-based measurements (Naito et al., 2014; NRA, 2014;  
259Yamashita and Itabashi, 2015; Miyazaki and Hayano, 2016; Wainwright et al.,  
2602017; Kinase et al., 2017). To account such systematic shift in Fig. 4, a linear  
261model was fitted with two parameters (i.e., slope and intercept) shown in  
262Table S1 and S2. In Fig. 3 and 4, the correlation coefficients are generally  
263higher than the data from Fukushima City presented in Wainwright et al.  
264(2017). This is due to the fact that the dose rates are higher in the  
265evacuation zone than Fukushima City, as discussed in Wainwright et al.  
266(2017).

267

268The three kinds of data were integrated using the developed method  
269(Wainwright et al., 2017). A series of integrated maps from 2014 to 2016 (50  
270m by 50 m resolution) are compared to the airborne survey datasets in Fig. 5  
271(The zoom-up figures are available in Fig. S1). Both airborne data and  
272integrated maps show that air dose rates are decreasing consistently across  
273the region over the two years, and that the region above  $3.8 \mu\text{Sv/h}$  is  
274shrinking. In general, the integrated maps (Fig. 5c-d) show more detailed and  
275finer-resolution heterogeneity than the original airborne data (Fig. 5a-c),  
276although the general trend is very similar. The systematic bias (or shift) in  
277the airborne data (Fig. 5a-c) is corrected in the integrated maps (Fig.5d-f).  
278For example, the area of above  $3.8 \mu\text{Sv/h}$  is  $72.8 \text{ km}^2$  in the integrated map  
279in 2016, which is significantly smaller than the one in the original airborne  
280survey ( $141.3 \text{ km}^2$ ). The overestimation is quite significant so that the region  
281above  $3.8 \mu\text{Sv/h}$  is larger in the airborne survey data in 2016 (Fig. 5c) than  
282the 2015 integrated map (Fig. 5e). Correcting such overestimation would be  
283important, since  $3.8 \mu\text{Sv/h}$  is considered to roughly correspond to an annual  
284exposure dose of 20 mSv and often used as the threshold value for policy  
285decision making.

286

287The performance of the integrated maps was confirmed by the validation  
288(Fig. 6), using one hundred points of the walk survey data excluded from the  
289estimation. Without the data integration, the airborne data at co-located  
290points (blue dots) exhibit larger scatters and a systematic bias compared to

291the co-located walk survey data. After the data integration, the predicted  
292values (based on our approach and the three datasets) are tightly distributed  
293around the one-to-one line and are mostly included in the 99% confidence  
294interval. The validation result (Fig. 6) shows that this method successfully  
295estimates the fine-resolution dose-rate map based on the spatially sparse  
296walk and car survey data and airborne data.

297

298Figure 7 shows the log-difference in the air dose rates between two  
299consecutive years calculated from the integrated maps shown in Fig. 5.  
300Although the east-west lines associated with the flight lines can be seen as  
301an artifact in the forested region, we can still see significant anthropologic  
302effects. The artifact is relatively small (5-10% of the dose rates) so that it is  
303noticeable only in this reduction map (Fig. 7): not in the integrated map or  
304airborne data (Fig. 5). The artifact was corrected within the urban or  
305cropland areas where the walk and car survey datasets are available.  
306Between 2014 and 2015, the Joban highway was opened with a fresh  
307pavement without contamination, which shows as a large reduction along  
308the north-south road in the southwest part of the domain (Fig. 7a). The  
309decontamination activity was known to be particularly active in the  
310southwest region of the domain (Tomioka Village). Between 2015 and 2016,  
311the decontamination was active in the northwestern region (Minami-soma  
312City), which can be seen in Fig. 7b. This is the first time that the  
313decontamination effect is visualized in the regional scale. After the



314Chernobyl accident, regional-scale decontamination was found to be  
315ineffective due to the re-contamination (Vovk et al., 1993). After the  
316Fukushima accident, extensive research and investigation have been made  
317in decontamination technologies and applications (Miyahara et al., 2012).  
318Our results show that the decontamination is quite effective to reduce the air  
319dose rates.

320

321The dose rate reduction of air dose rates was computed at each pixel, and  
322summarized in each land-use class as the median and five and ninety-five  
323percentiles (Table 1). The urban area has a large reduction as well as a large  
324variability in the reduction, which suggests the effect of paved surfaces on  
325the mobility of radiocesium (e.g. roads) as well as anthropologic effects (e.g.,  
326decontamination and traffic) consistent with previous studies (e.g., Kinase et  
327al., 2014; Kinase et al., 2017; Saito, 2016). The reduction is larger than the  
328computed median values in each land-use type based on the data-driven  
329model in Kinase et al. (2017). This suggests that the regional-scale ecological  
330half-life for the fast and slow elimination components could be smaller or the  
331fast elimination fraction could be larger than the values used in Kinase et al.  
332(2017). In addition, the reduction is smaller in 2015-2016 than 2014-2015,  
333suggesting the decreasing fraction of  $^{134}\text{Cs}$ . We expect the reduction rate  
334would decrease in the future, although the reduction would remain larger  
335than the physical decay due to the radiocesium transport in the  
336environment.

337

338 Figure 8 shows the predicted maps in 2026 based on the 2016 integrated  
339 map (the enlarged version is available in the supporting information as  
340 Figure S2). The prediction is based on the assumptions that the ecological  
341 decay continues at the current rate, and that the decontamination is not  
342 considered. The air dose rates continue to decrease, and the region above  
343  $3.8 \mu\text{Sv/h}$  is predicted to shrink significantly in 2026. Since we used the  
344 parameters from Kinase et al. (2017), the actual reduction could be faster  
345 than this map. Although there is still a remaining area above  $3.8 \mu\text{Sv/h}$ , this  
346 area is almost fully contained within the non-residential forested zone. The  
347 area above  $3.8 \mu\text{Sv/h}$  is  $14.2 \text{ km}^2$ , 97.8 % of which is in the forested area.  
348 The effectiveness of remediation in the forested region has been debated  
349 since the accident, since the soil, plant and/or litter removal leads to  
350 significant ecological disturbance (Ayabe et al., 2017). Globally, there has  
351 been a paradigm shift in environmental remediation from an approach of  
352 intense soil removal and treatment to one of passive remediation or natural  
353 attenuation (Ellis and Hadley, 2009). Such sustainable remediation considers  
354 *net environmental impacts* including ecological disturbances, waste  
355 generation and energy usage. Also, it promotes longer institutional control  
356 with alternative end-use of the restricted land. Our prediction - that  
357 contamination will be limited within the non-residential forested zone in 10  
358 years - could have an impact on decontamination planning in the sustainable  
359 remediation framework. For example, focusing decontamination in the

360residential areas would be more effective for the residents' return while  
361avoiding ecological disturbances in forested regions and reducing cost and  
362waste.

363

#### 364**4. Conclusion**

365In this study, we characterized the regional-scale changes in the air dose  
366rates within the evacuation designated area around the Fukushima Nuclear  
367Power Plant. We first applied the Bayesian data integration approach to  
368create the integrated maps of air dose rates in 2014, 2015 and 2016, based  
369on multi-type multiscale datasets available in the region. We quantified the  
370ecological half-life and dose-rate reduction depending on land-use types,  
371then coupled the integrated map with the data-driven predictive model to  
372predict the future radiation air dose rates with increased accuracy.

373

374This was the second demonstration of our Bayesian data-integration  
375approach developed by Wainwright et al. (2017) in a higher-dose region and  
376in the larger spatial scale. The results have again shown that the proposed  
377method was effective to integrate multiscale, multi-type dose-rate  
378measurements, and also to create the high-resolution air dose rates over the  
379large spatial extent. The validation has confirmed a consistent performance  
380of this method over these three years. Integrated maps captured more  
381detailed spatial heterogeneity than the regional airborne survey data, and  
382corrected a significant positive bias in the airborne survey.

383

384The integrated maps enable us to visualize the temporal changes of air-dose  
385rates in the regional scale. The dose rate reduction was computed based on  
386these integrated maps, and the reduction was shown to be smaller in the  
387forested region than the other land-use types, which is consistent with  
388previous studies (Kinase et al., 2014; Saito, 2016). The integrated maps were  
389particularly powerful in identifying anthropologic effects such as the re-  
390opening of roads and effects of decontamination. In addition, the predictive  
391modeling results showed that by 2026, the air dose rates would continue to  
392decrease, and the area above 3.8  $\mu\text{Sv/h}$  would be almost fully contained  
393within the non-residential forested zone.

394

### 395**Acknowledgement**

396The environmental monitoring data in this study were acquired during the  
397projects commissioned by the Japan Nuclear Regulatory Agency. We thank  
398the people who contributed to collecting the data and compiling them into  
399the JAEA database. Funding for this work was provided by Japan Atomic  
400Energy Agency under Award No. AWD00000626, as part of Work for Others  
401funding from Berkeley Lab, provided by the U.S. Department of Energy under  
402Contract No. DE-AC02-05CH11231.

403

404**Reference:**

405Andoh, M., Nakahara, Y., Tsuda, S., Yoshida, T., Matsuda, N., Takahashi, F., ...

406& Takamiya, K. (2015). Measurement of air dose rates over a wide area

407around the Fukushima Dai-ichi Nuclear Power Plant through a series of car-

408borne surveys. *Journal of environmental radioactivity*, 139, 266-280.

409

410Ayabe, Y., Hijii, N., & Takenaka, C. (2017). Effects of local-scale

411decontamination in a secondary forest contaminated after the Fukushima

412nuclear power plant accident. *Environmental Pollution*, 228, 344-353.

413

414Ellis, D. E., and Hadley, P. W. (2009). Sustainable Remediation White Paper -

415Integrating Sustainable Principles, Practices, and Metrics Into Remediation

416Projects. *Remediation Journal*, 19(3), 5-114.

417<https://doi.org/10.1002/rem.20210>.

418

419Fukushima Prefectural Government,

420<http://www.pref.fukushima.lg.jp/site/portal-english/en03-08.html>, retrieved

421on December 19<sup>th</sup>, 2017.

422

423Kinase, S., Takahashi, T., Sato, S., Sakamoto, R., & Saito, K. (2014).

424Development of prediction models for radioactive caesium distribution within

425the 80-km radius of the Fukushima Daiichi nuclear power plant. *Radiation*

426protection dosimetry, 160(4), 318-321.

427

428Kinase, S., Sato, S., Sakamoto, R., Yamamoto, H., & Saito, K. (2015). Changes  
429in ambient dose equivalent rates around roads at Kawamata town after the  
430Fukushima accident. *Radiation protection dosimetry*, 167(1-3), 340-343.

431

432Kinase, S., Takahashi, T., & Saito, K. (2017). Long-term predictions of  
433ambient dose equivalent rates after the Fukushima Daiichi nuclear power  
434plant accident. *Journal of Nuclear Science and Technology*, 1-10.

435

436Kitamura, A., Yamaguchi, M., Kurikami, H., Yui, M., & Onishi, Y. (2014).  
437Predicting sediment and cesium-137 discharge from catchments in eastern  
438Fukushima. *Anthropocene*, 5, 22-31.

439

440Matsuda, N., Mikami, S., Sato, T., & Saito, K. (2017). Measurements of air  
441dose rates in and around houses in the Fukushima Prefecture in Japan after  
442the Fukushima accident. *Journal of environmental radioactivity*, 166, 427-  
443435.

444

445Malins, A., Kurikami, H., Nakama, S., Saito, T., Okumura, M., Machida, M., &  
446Kitamura, A., Evaluation of ambient dose equivalent rates influenced by  
447vertical and horizontal distribution of radiocesium in soil in Fukushima  
448Prefecture. *Journal of Environmental Radioactivity*, 151, 38-49, 2016.

449

450Miyazaki, M., & Hayano, R. (2016). Individual external dose monitoring of all  
451citizens of Date City by passive dosimeter 5 to 51 months after the  
452Fukushima NPP accident (series): 1. Comparison of individual dose with  
453ambient dose rate monitored by aircraft surveys. *Journal of Radiological*  
454*Protection*, 37(1), 1.

455

456Mikami, S., Maeyama, T., Hoshide, Y., Sakamoto, R., Sato, S., Okuda, N., ... &  
457Saito, K. (2015a). The air dose rate around the Fukushima Dai-ichi Nuclear  
458Power Plant: its spatial characteristics and temporal changes until December  
4592012. *Journal of environmental radioactivity*, 139, 250-259.

460

461Mikami, S., Maeyama, T., Hoshide, Y., Sakamoto, R., Sato, S., Okuda, N., ... &  
462Fujiwara, M. (2015b). Spatial distributions of radionuclides deposited onto  
463ground soil around the Fukushima Dai-ichi Nuclear Power Plant and their  
464temporal change until December 2012. *Journal of environmental*  
465*radioactivity*, 139, 320-343.

466

467Miyahara, K., Tokizawa, T., & Nakayama, S. (2012). Overview of the results of  
468Fukushima decontamination pilot projects. Japan Atomic Energy Agency.

469

470Naito, W., Uesaka, M., Yamada, C., & Ishii, H. (2014). Evaluation of dose from  
471external irradiation for individuals living in areas affected by the Fukushima

472Daiichi Nuclear Plant accident. *Radiation protection dosimetry*, 163(3), 353-  
473361.

474

475Nuclear Regulation Authority (2014), Characterizing the long-term effects of  
476radionuclide deposition after the Fukushima Dai-ichi Nuclear Power Plant  
477accident, Japanese. Available from:

478<http://radioactivity.nsr.go.jp/ja/list/504/list-1.html>.

479

480Peles, J. D., Smith, M. H., & Brisbin, I. L. (2002). Ecological half-life of <sup>137</sup>Cs  
481in plants associated with a contaminated stream. *Journal of environmental*  
482*radioactivity*, 59(2), 169-178.

483

484Saito, K., & Onda, Y. (2015). Outline of the national mapping projects  
485implemented after the Fukushima accident.

486

487Saito, K., Tanihata, I., Fujiwara, M., Saito, T., Shimoura, S., Otsuka, T., ... &  
488Kinouchi, N. (2015). Detailed deposition density maps constructed by large-  
489scale soil sampling for gamma-ray emitting radioactive nuclides from the  
490Fukushima Dai-ichi Nuclear Power Plant accident. *Journal of environmental*  
491*radioactivity*, 139, 308-319.

492

493Saito, K. (2016). Features of Exposure Doses to the Public due to the  
494Fukushima Accident. *Global Environmental Research*, 20, 67-72.



495

496 Seki, A., Saito, O., Nago, H., Suzuki, K., Tomishima, K., Saito, K., & Takemiya,  
497 H. (2014). Development of a software platform for providing environmental  
498 monitoring data for the Fukushima Daiichi nuclear accident. *Radiation  
499 protection dosimetry*, 164(1-2), 97-102.

500

501 Takahashi, M., Nasahara, K. N., Tadono, T., Watanabe, T., Dotsu, M.,  
502 Sugimura, T., and Tomiyama, N. (2013, July). JAXA High Resolution Land-Use  
503 and Land-Cover Map of Japan. In *Geoscience and Remote Sensing  
504 Symposium (IGARSS), 2013 IEEE International* (pp. 2384-2387). IEEE.

505

506 Tanaka, S. (2012), Accident at the Fukushima Dai-ichi Nuclear Power Stations  
507 of TEPCO —Outline & lessons learned, *Proc. Jpn. Acad. Ser. B Phys. Biol. Sci.*,  
508 88(9): 471–484.

509

510 Tanigaki, M., Okumura, R., Takamiya, K., Sato, N., Yoshino, H., & Yamana, H.  
511 (2013). Development of a car-borne  $\gamma$ -ray survey system, KURAMA. *Nuclear  
512 Instruments and Methods in Physics Research Section A: Accelerators,  
513 Spectrometers, Detectors and Associated Equipment*, 726, 162-168.

514

515 Tanigaki, M. (2016). Development and Operation of a Carborne Survey  
516 System, KURAMA. In *Radiological Issues for Fukushima's Revitalized Future*  
517 (pp. 111-120). Springer Japan.

518

519Torii, T., Y. Sanada, T. Sugita, A. Kondo, Y. Shikaze and Y. Urabe,  
520Investigation of Radionuclide Distribution Using Aircraft for Surrounding  
521Environmental Survey from Fukushima Daiichi Nuclear Power Plant, JAEA-  
522Technology 2012-036, (in Japanese), 2012.

523

524Tsuda, S., Yoshida, T., Tsutsumi, M., & Saito, K. (2015). Characteristics and  
525verification of a car-borne survey system for dose rates in air: KURAMA-II.  
526Journal of environmental radioactivity, 139, 260-265.

527

528Yamashita, T., & Itabashi, K. (2015). Technical support of decontamination  
529projects and communication activity for residents to understand radiation.  
530Activities for the environmental recovery by JAEA (3). Nippon Genshiryoku  
531Gakkai-Shi, 57(10), 656-661.

532

533Yasutaka, T., Iwasaki, Y., Hashimoto, S., Naito, W., Ono, K., Kishimoto, A., ...  
534& Nakanishi, J. (2013). A GIS-based evaluation of the effect of  
535decontamination on effective doses due to long-term external exposures in  
536Fukushima. Chemosphere, 93(6), 1222-1229.

537

538Vovk, I. F., Blagoyev, V. V., Lyashenko, A. N., & Kovalev, I. S. (1993).  
539Technical approaches to decontamination of terrestrial environments in the  
540CIS (former USSR). Science of the total environment, 137(1-3), 49-63.

541

542Wainwright, H. M., Seki, A., Chen, J., & Saito, K. (2017). A multiscale Bayesian  
543data integration approach for mapping air dose rates around the Fukushima  
544Daiichi Nuclear Power Plant. *Journal of environmental radioactivity*, 167, 62-  
54569.

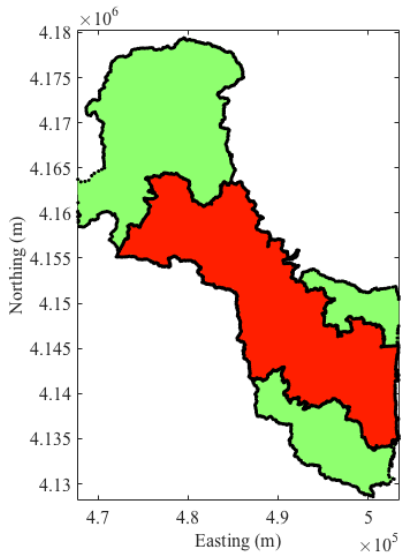
546

547Wei, L., Kinouchi, T., Yoshimura, K., & Velleux, M. L. (2017). Modeling  
548watershed-scale <sup>137</sup>Cs transport in a forested catchment affected by the  
549Fukushima Dai-ichi Nuclear Power Plant accident. *Journal of Environmental*  
550*Radioactivity*, 171, 21-33.

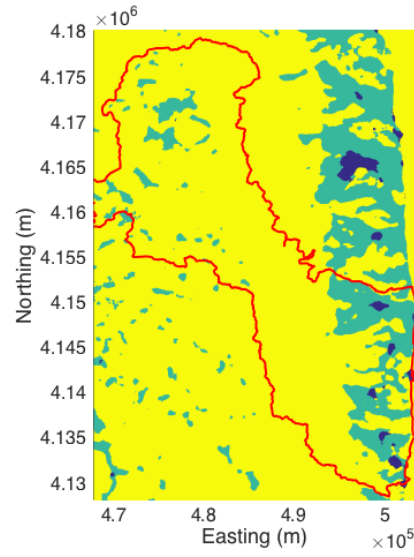
551

552Wikle, C.K., R.F. Milliff, D. Nychka and L. M. Berliner, Spatiotemporal  
553hierarchical Bayesian modeling: tropical ocean surface winds, *J. Am. Stat.*  
554*Assoc.*, 96(454), 382-397, 2001.

555



556

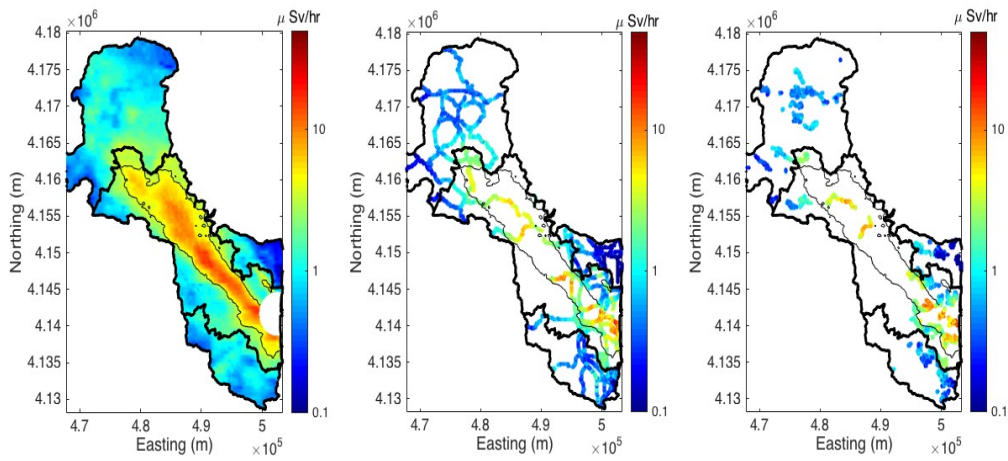


(b)

558(a)

559 Figure 1. (a) Evacuation designated area and (b) land cover types (blue =  
 560 urban, green = cropland and yellow = forest). In (a), the red region is the  
 561 evacuation designated area as of April 2017. The green region is where the  
 562 restriction order was lifted in April 2017.

563



564

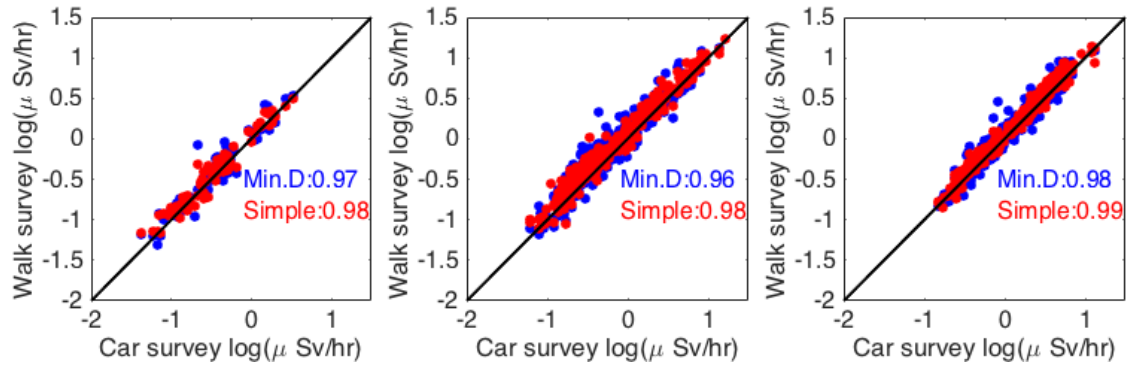
565 (a)

(b)

(c)

566 Figure 2. Comparison among different types of datasets in 2016: (a) airborne  
 567 survey, (b) car survey and (c) walk survey data. The thin black contour lines  
 568 are the threshold of 3.8  $\mu\text{Sv/h}$ . The thick black lines are different zones within  
 569 the evacuation designated area shown in Fig. 1a.

570



571

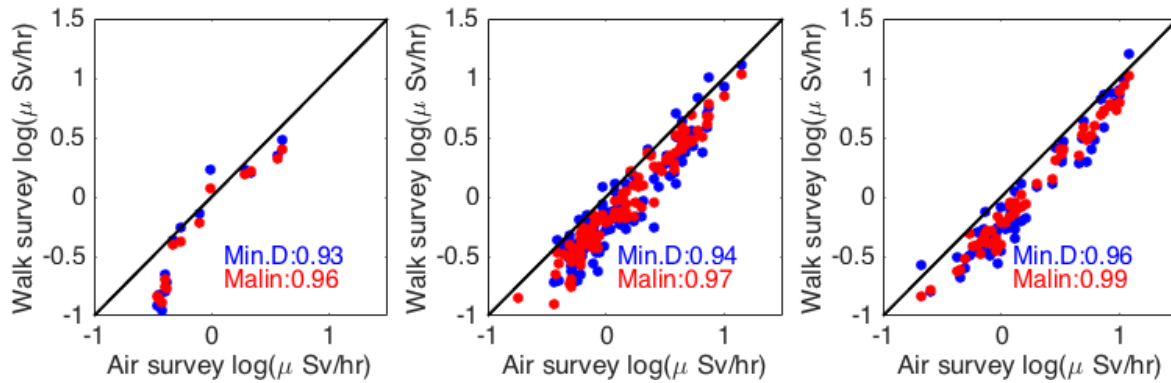
572(a)

(b)

(c)

573 Figure 3. Comparison between the car and walk survey data: (a) urban, (b)  
 574 cropland, and (c) forest areas in the 2016 data. The blue circles (“Min. D”)  
 575 are the co-located points identified by the minimum distance. The red circles  
 576 (“Simple”) are the average of the walk survey points using the simple  
 577 average. In each plot, the correlation coefficients are shown.

578



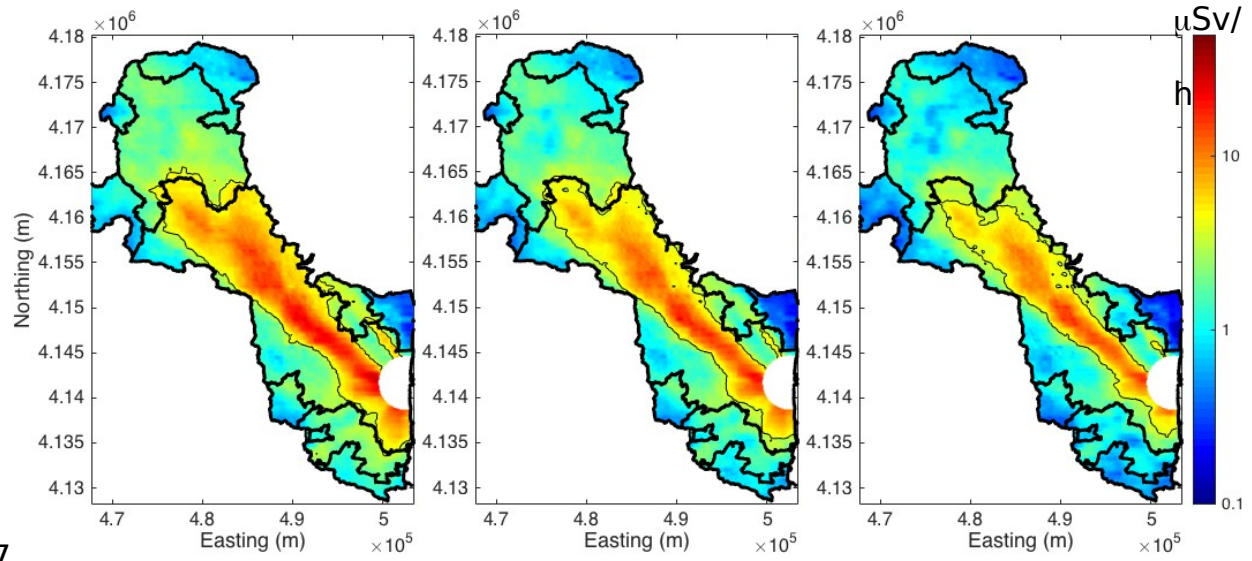
579

580(a)

(b)

(c)

581Figure 4. Comparison between the air and walk survey data in: (a) urban, (b)  
 582cropland, and (c) forest and areas in the 2016 data. The blue circles (“Min.  
 583D”) are the co-located points identified by the minimum distance. The red  
 584circles (“Malin”) are the average of the walk survey points using the weights  
 585computed by the radiation transport simulation. In each plot, the correlation  
 586coefficients are shown.

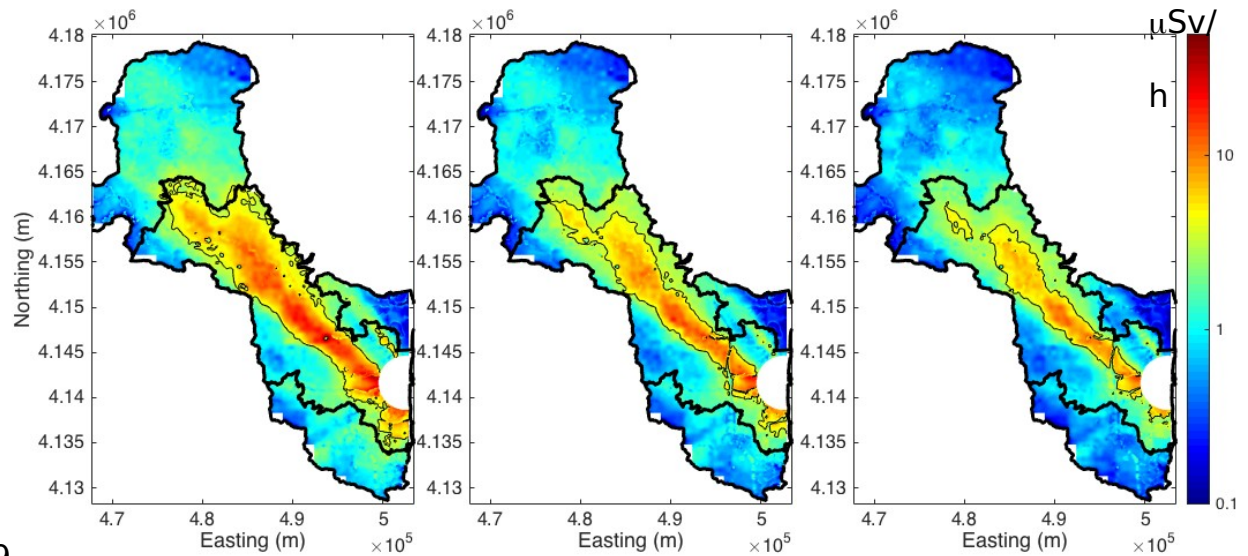


587

588(a)

(b)

(c)



589

590(d)

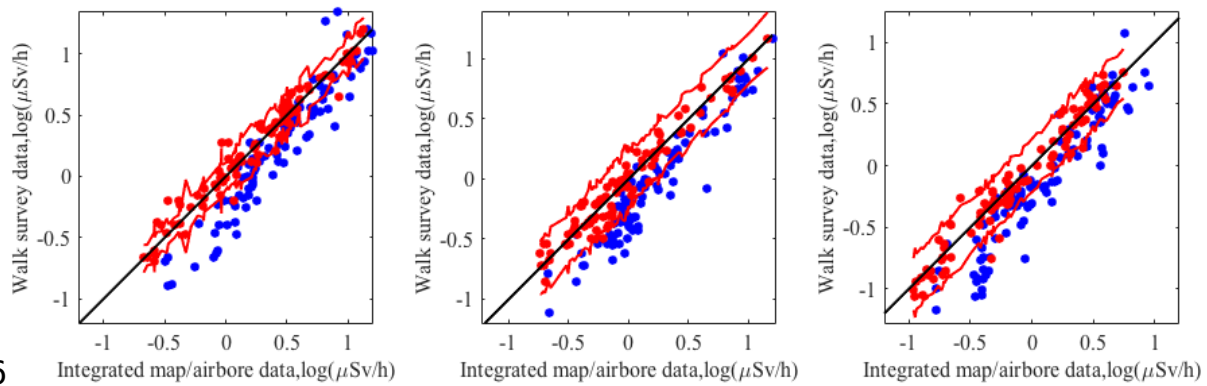
(e)

(f)

591 Figure 5. Temporal evolution of (a-c) airborne survey data and (d-f)  
 592 integrated maps in (a, d) 2014, (b, e) 2015 and (c, f) 2016. The thin black  
 593 contour lines are the threshold of  $3.8 \mu\text{Sv/h}$ . The thick black lines are  
 594 different zones within the evacuation designated area shown in Fig. 1a.







596

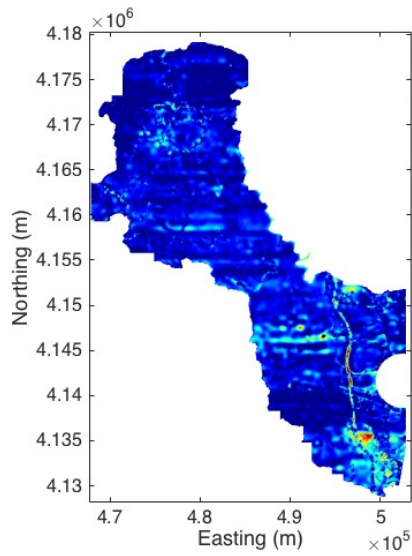
597(a)

(b)

(c)

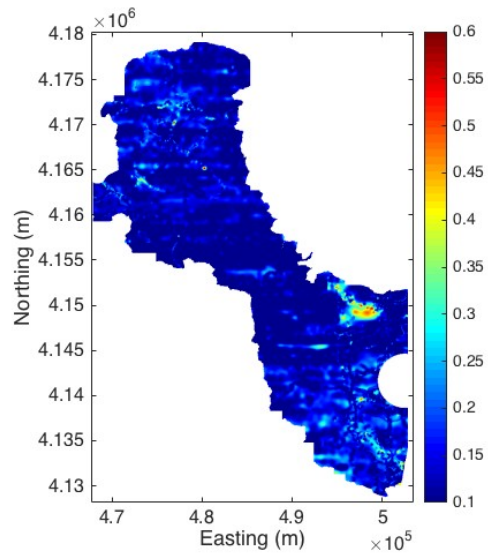
598Figure 6. Validation results: comparison of the log-transformed walk survey  
 599data to the integrated map (red circles) and to the co-located airborne data  
 600(blue circles) at the walk-survey data locations not used for the estimation in  
 601(a) 2014, (b) 2015 and (c) 2016. The red dots represent the predicted values  
 602based on the data integration method; the blue dots are the co-located  
 603airborne data without using the integration. The black line is the one-to-one  
 604line; the red lines are the 99% confidence intervals.

605



606

607 (a)

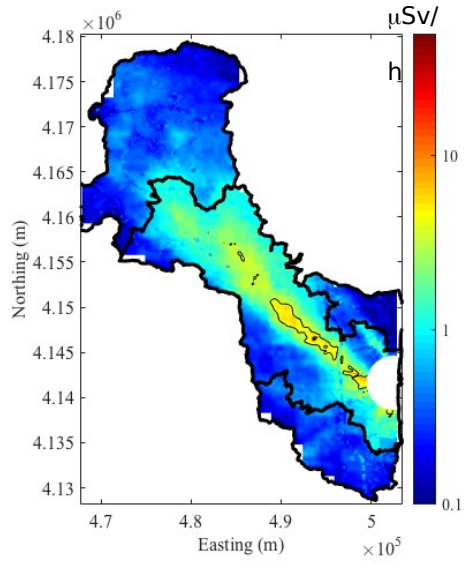


(b)

608 Figure 7. Log-difference of the air dose rates between (a) 2014 - 2015 and

609 (b) 2015 - 2016.

610



611

612

613 Figure 8. Predicted air dose rate in 2026 based on the integrated map. The  
614 thin black contour lines are the threshold of 3.8  $\mu\text{Sv/h}$ . The thick black lines  
615 are different zones within the evacuation designated area.

616

617 Table 1. Median reduction in the air dose rate within each land-use type,  
 618 along with the range of the five and ninety-five percentiles in the prentices.  
 619 The reduction was defined by the ratio of air dose rates between the two  
 620 years at each pixel.

	2014-2015	2015-2016	2014-2016
Urban	0.68 (0.46 - 0.95)	0.74 (0.40 - 1.00)	0.50 (0.25 - 0.75)
Cropland	0.70 (0.46 - 0.89)	0.72 (0.47 - 0.93)	0.50 (0.28 - 0.71)
Forest	0.72 (0.57 - 0.86)	0.78 (0.63 - 0.95)	0.57 (0.42 - 0.70)
Kinase	0.83 (0.79 - 0.86)	0.86 (0.82 - 0.86)	0.72 (0.65 - 0.72)
model(forest)*	0.87	0.89	0.77
Kinase model (others)	0.83 (0.78 - 0.87)	0.86 (0.81 - 0.89)	0.72 (0.64 - 0.77)

621\* Kinase et al. (2017)

622